Intrusive STM imaging

Nicolas Boulanger-Lewandowski* and Alain Rochefort†
Département de génie physique and Regroupement québécois sur les matériaux de pointe (RQMP), École Polytechnique de Montréal, Montréal, Québec H3C 3A7, Canada
(Received 23 September 2010; revised manuscript received 12 January 2011; published 15 March 2011)

An interactive scanning tunneling microscopy (STM) simulator has been designed to efficiently compute the effects of chemical and structural modifications of adsorbed species on resulting STM images. Our general approach is based on first-order perturbation theory that takes into account different tip geometries. In our intrusive STM imaging strategy, we consider small variations such as substitutions, vacancies, functionalizations, and molecular reorganizations from a reference system. First, we show that our perturbation theory approach can provide STM images that are qualitatively similar to those of a more rigorous electron scattering technique based on the Landauer-Büttiker formalism for the case of adsorbed tetracyanoethylene on a Cu(100) single crystal. Second, we demonstrate that the efficiency of Bardeen and Tersoff-Hamann approaches to generate STM images can be substantially improved by exploiting different algorithms to evaluate the tunnel current and to deal with large-scale eigenvalue problems. Following our general intrusive strategy, we have reduced the computing time to generate an STM image of a modified system by about an order of magnitude with respect to the reference image. The shape and position of the contrasts of the STM image evaluated in the context of intrusion are virtually identical to an image computed without intrusive features but within a considerably smaller computing time.

DOI: 10.1103/PhysRevB.83.115430 PACS number(s): 68.37.Ef, 71.15.−m, 73.63.Rt, 73.20.At

I. INTRODUCTION

Scanning tunneling microscopy (STM)[1,2] is an essential technique of nanoscience to obtain atomic resolution images of adsorbed species. STM has found applications in physics, chemistry, and biology.[3] It is one the few nondestructive techniques that can image *in situ* growth and adsorption processes with an atomic resolution.[4–7] It can even probe electromagnetic structures,[8,9] collective excitation states,[10] and interference patterns caused by impurities.[11,12] STM is not strictly used to perform a passive observation of surfaces species, but also to manipulate individual atoms and molecules in a *bottom-up* fashion to construct nanoscale systems.[13,14] Finally, it can help to provoke complex chemical chain reactions by bringing different species together followed by voltage pulses at specific locations.[15] The possibility for the microscope to discriminate between the different products of the reaction is then crucial.

In many STM experiments, the chemical composition of the sample plays an important role on the observed contrasts. Ideally, the coherence of shapes and sizes suffices to identify the molecular species expected on the substrate,[16,17] but in the case of complex reactions or mixtures of adsorbates, identifying a given species is more difficult.[18–23] An obvious reason is that different adatoms may show completely different STM profiles[24–26] and vary among different adsorption sites.[27] Beyond the famous example in which the adsorption sites of benzene on Pt(111) have been clearly revealed and described,[28] other systems such as CO/Pt(111) have revealed more specific features associated with the intrinsic electronic properties of the adsorbate.[13,29]

On the other hand, the withdrawal or substitution of an atom or group of atoms can be probed by STM at the single-molecule level.[30] Lauhon and Ho[31] have shown that benzene-d_6 (C_6D_6), a dissociation product of benzene induced by a tunneling current pulse, and pyridine (C_5H_5N) produce different STM contrasts. The dehydrogenation products of benzene were more lately identified as phenyl (C_6H_5) and benzyne (C_6H_4).[32,33] Different STM studies on fluorobenzene (C_6H_5F),[34] chlorobenzene (C_6H_5Cl),[35] and iodobenzene (C_6H_5I)[36] clearly revealed the importance of chemical substitutions. Chemical conformation plays a significant role on the nature of the STM contrasts as seen for the isomers of monomethylazulene ($C_{11}H_{10}$), naphtalene, and azulene ($C_{10}H_8$).[37] In addition, electronic properties of carbon nanotubes (CNTs) can be modulated by introducing point defects for which fluctuations of the wave function can be probed with STM.[38,39]

Despite the atomic resolution obtained with STM, the interpretation of raw images is not always trivial. Precise surface structures are usually determined by a successive comparison of STM simulations performed on a series of molecular models of fixed surface species to experimental results until the simulations can reproduce the main features of experimental data.[40–42] Prior to the STM simulations, computationally demanding electronic structure calculations usually have to be carried out in order to obtain the surface models and the related wave function.

In the present work, we propose a more interactive and rapid approach that allows us to directly modify the chemical composition or surface structure of the molecular model, and to simultaneously follow its influence on the resulting STM image without performing further fastidious electronic structure calculations on the whole system. We need to introduce the concept of *intrusion* where an external user performs a chemical or physical modification on the original STM junction model. The more important part in this *intrusion* is associated with an ideal real-time observation of these modifications on the resulting STM images. Such feature would facilitate the determination of the adsorbate structure, including chemical composition, surface reconstruction, adsorption site and geometry, as well as the apex constitution, the tip angle, etc.[43] Furthermore, the possibility of modifying the chemical composition of a surface species

and to simultaneously obtain its electronic properties from the STM image opens an interesting route for materials design.

The major contribution of our work is an efficient combination of electronic structure and electronic transport methods to rapidly produce accurate STM images. To our knowledge, very few works have been published on such a general approach, and they still only implement a subset of our own.[44,45] We are also proposing a method to compute the updated STM image after a perturbation, which is much faster than if the image is computed from scratch. The next sections present the formalism used for building the STM model using truncated clusters, for diagonalizing the tunnel junction system with direct and iterative methods, for evaluating the tunneling current using the Bardeen perturbative method, and for optimizing the STM image update after an intrusion. We then validate the quality of our approach in terms of physical description, performance, relevance of the image update procedure, and scaling to system size on model systems such as adsorbed molecular chains, benzene derivatives, and CNTs of various sizes.

II. METHODOLOGY

A. STM model

Although the magnitude of the tunneling current I depends on the complex coupling between the density of states (DOS) of the sample and the tip within the tunneling barrier region, it can be roughly associated with the surface topography $z'(x,y)$:

$$I(\mathbf{r},V) \sim V \exp[-\alpha(z-z')], \tag{1}$$

where $\mathbf{r} \equiv (x,y,z)$ is the position of the tip apex, V is the applied bias to the tip-sample couple, and α is related to the work function of the sample.

When the sample-tip distance is sufficiently large ($z > 5$ Å), the electronic structure of both parts can be obtained separately, and perturbation theory can be used to describe their interactions in a tunnel junction. Both sample and tip are described in our STM model (Fig. 1) by a semi-infinite contact that is attached to a molecular cluster which encompasses a surface region and a portion of the actual substrate to account for (1) potential surface effects such as band bending[46] and (2) the chemical environment in the vicinity of the adsorbate.[47]

The coupling of the cluster to the contact can be exactly described[48] by a self-energy term $\Sigma(E)$ in the Hamiltonian, and this effect shifts the discrete states E_i of the isolated cluster by δE_i and spectrally broadens them by γ_i. The broadening is related to the escape rate of an electron in the contact in a state i, and can be estimated to $\gamma_i \simeq 0.1$–1.0 eV.[49] This value can be evaluated from first-order perturbation theory.[50]

Assuming that $\delta E_i \ll E_i$, the local density of states (LDOS) $\rho(E,\mathbf{r})$ of the entire system can be approximated by a Gaussian broadening γ_i similar to the discrete LDOS of the isolated cluster:

$$\rho_i(E,\mathbf{r}) = \frac{1}{\gamma_i\sqrt{\pi}}|\Psi_i(\mathbf{r})|^2 \exp - \left(\frac{E-E_i}{\gamma_i}\right)^2, \tag{2}$$

$$\rho(E,\mathbf{r}) = \sum_i \rho_i(E,\mathbf{r}). \tag{3}$$

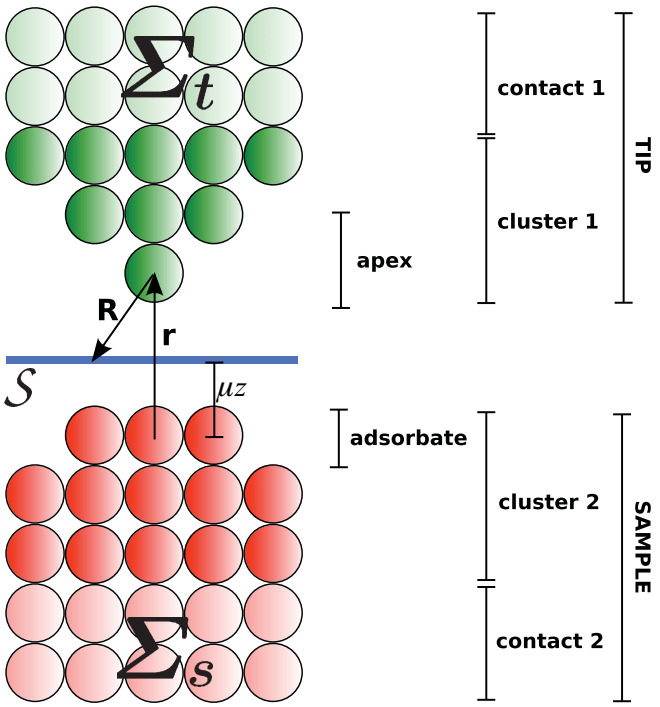

FIG. 1. (Color online) The sample-tip junction in the STM model, where $\mathbf{r} \equiv (x,y,z)$ denotes the position of the tip apex with respect to the sample origin, $\mathbf{R} \equiv (X,Y,Z)$ represents a point on the separation surface $\mathcal{S}$ with respect to the tip apex, and $Z \equiv (1-\mu)z$. The effects of both semi-infinite contacts are represented by their self-energies $\Sigma_s(E)$ and $\Sigma_t(E)$.

This approach allows us to efficiently describe both resonant ($\gamma_i \ll |E_i - E_{i+1}|$) and band ($\gamma_i \simeq |E_i - E_{i+1}|$) transport.[46] Note that computing the precise form of the LDOS spectrum would require a radical change of focus to consider the energy E as the independent variable instead of finding the resonant energies E_i (eigenvalues) of the system. Such approach has been used by several authors to compute wave functions from Green's functions,[51,52] and should give a more accurate description of the contacts. Nevertheless, the choice of using atomic clusters allows us to more efficiently construct the molecular orbitals using the resonant states (computed once). The use of atomic clusters introduces only a few qualitative changes in the final electronic structure, while the increase in speed of the evaluation of matrix elements M_{st} is significantly enhanced.

In order to reduce the computing time to generate an STM image, the electronic structures were evaluated with the extended Hückel theory (EHT).[53] Such theory may be considered as an improved tight-binding method since it explicitly evaluates overlap matrix elements. EHT has been successfully used at several occasions in electron transport calculations,[50,54] and more specifically in STM simulations.[55–57] EHT describes valence electrons by a linear combination of N atomic orbitals (LCAO):

$$\Psi_i = \sum_{j=1}^{N} \chi_{ij}\psi_j, \tag{4}$$

where Ψ_i are the molecular wave functions with energy E_i, ψ_j are the basis functions, and χ_{ij} are the coefficients. Hence, the time-independent Schrödinger equation becomes a matrix generalized eigenvalue problem:

$$H\chi = SE\chi, \tag{5}$$

where H is the Hamiltonian matrix and S is the symmetric positive-definite overlap matrix ($S_{ij} \equiv \langle \psi_i \mid \psi_j \rangle$). EHT evaluates the Hamiltonian matrix elements H_{ij} from parametrized on-site energies H_{ii} and are proportional to the overlap integral S_{ij}:

$$H_{ij} = K_{ij}\left(\frac{H_{ii} + H_{jj}}{2}\right) S_{ij}, \tag{6}$$

where K_{ij} is the adimensional Hückel constant. It is traditionally fixed at 1.75 for atomic and molecular species but it can also be varied for every atomic orbital pair ($K_{ij} \equiv \frac{K_i + K_j}{2}$) to make the parametrization more flexible.[54]

This work uses basis sets of double-ζ Slater-type orbitals (STO) of the following form:

$$\psi_i(\mathbf{C}_i + \mathbf{r}) = Y_m^l(\hat{\mathbf{r}}) r^{n-1}\left(c_1 e^{-\zeta_1 r} + c_2 e^{-\zeta_2 r}\right), \tag{7}$$

where $\mathbf{r}$ is the position relative to the atomic center $\mathbf{C}_i$, Y_m^l are the spherical harmonics, n, l, and m are the quantum numbers, and $\hat{\mathbf{r}} \equiv \mathbf{r}/r$. The exponential radial part of STOs describes well the expected shape of the wave function near the nuclei and in vacuum. This feature is important to accurately model the tunneling barrier where the potential is roughly constant.

Using our list of N basis functions parametrized by

$$C_x,\ C_y,\ C_z,\ n,\ m,\ l,\ c_1,\ c_2,\ \zeta_1,\ \zeta_2,\ H_{ii},\ K_i, \tag{8}$$

we can construct the overlap matrix by blocks of size $(2l_1 + 1) \times (2l_2 + 1)$ by exploiting commonalities between classes of atomic orbitals $\langle \mathbf{C}_1, n_1, l_1 \mid \mathbf{C}_2, n_2, l_2 \rangle$.[58,59] All parameters in (8) were evaluated from DFT calculations following the procedure of Cerdá and Soria.[60] The Hamiltonian matrix follows directly from (6).

In this semiempirical model, we neglect matrix entries for which $|\mathbf{C}_i - \mathbf{C}_j| \geqslant$ 8–10 Å and when $S_{ij} \leqslant 10^{-7}$. For large systems where the number of nonzero matrix elements $n_{nz} = O(N)$ is small compared to N^2, it becomes necessary to store S and H as sparse matrices.

B. Diagonalization

In STM simulation, diagonalization methods can be used to compute the surface states that contribute to the tunneling current in a specific energy window. This window is located near the Fermi level E_F and depends on the applied bias V_0, the bias range $[V_1, V_2]$, the states broadening γ_i, and the temperature T as

$$E_F^{(s)} + V_a - 3\gamma_s - 3k_BT \leqslant E_i^{(s)} \leqslant E_F^{(s)} + V_b + 3\gamma_s + 3k_BT, \tag{9}$$

$$E_F^{(t)} - V_b - 3\gamma_t - 3k_BT \leqslant E_i^{(t)} \leqslant E_F^{(t)} - V_a + 3\gamma_t + 3k_BT, \tag{10}$$

where $V_a = \min(V_0, V_1, V_2, 0)$, $V_b = \max(V_0, V_1, V_2, 0)$. Within the TH approximation in a spectroscopic mode (dI/dV), the boundaries are, rather, $V_a = \min(V_0, V_1, V_2)$ and $V_b = \max(V_0, V_1, V_2)$ since only states with $E_i^{(s)} \simeq E_F^{(s)} + eV$ contribute to the differential conductance $[dI/dV(\mathbf{r}, V)]$. The inclusion of the terms $3\gamma_i$ and $3k_BT$ in Eqs. (9) and (10) ensures that states outside the energy window have a negligible Fermi factor $F(V)$ [Eq. (15)] for all considered biases V. This technical detail will become clearer in the next subsection.

The generalized symmetric-definite eigenvalue problem in (5) is usually solved by the following direct procedure:[61] (i) reduction to a standard eigenvalue problem, e.g., $CX = EX$, (ii) a Householder tridiagonal decomposition $Q^TCQ = T$ where Q is orthogonal and T is tridiagonal, (iii) the iterative symmetric QR algorithm to find the eigenvalues E_i of T, and (iv) the inverse iteration to find the eigenvectors X. In order to only compute the eigenvalues lying in a predetermined range, step (iii) can be performed by a bisection method. The Sturm sequence can be used to compute eigenvalues E_i of given indices i, assuming the E_i are sorted. Both methods are implemented in the LAPACK library,[62] but a slight modification of the master drivers is necessary to combine both. Recall that we are interested in an energy window of predetermined range around the Fermi level which is known only by its index. The zero-based energy index of the Fermi level E_F for a system of n_e paired electrons is defined by the integer part of $(n_e - 1)/2$.

The generalized symmetric-definite eigenvalue problem defined in (5) can also be solved by the iterative Lanczos method[63] as implemented in the ARPACK library.[64] This method is a sophisticated version of the power method in which it only needs the *action* of the H and S matrices on a vector q, an efficient operation in $O(n_{nz})$ for sparse matrices. The scalar Lanczos algorithm iteratively determines the basis vectors of a fixed size Krylov subspace until it eventually becomes invariant under multiplication by $S^{-1}H$. Applying repeatedly $S^{-1}Hq$ would yield the highest magnitude E_i, but by using the well known shift-invert spectral transformation $S^{-1}H \to (S^{-1}H - E_0 I)^{-1}$, the highest magnitude eigenvalues of the shifted matrix correspond to the original eigenvalues E_i closest to E_0, typically chosen in the center of the energy window near E_F. The action needed for every iteration becomes

$$(H - E_0 S)^{-1} Sq = x, \tag{11}$$

which is a matrix-vector product and a solution of a system of linear equations. We used a direct LU factorization[65] of the $H - E_0 S$ term to solve (11). The L and U factors can be reused every cycle for the different right terms Sq. Note that H, S, and $H - E_0 S$ have the same distribution of nonzero elements according to (6). The factorization process retains a maximum of sparsity in the resulting L and U matrices. However, this method requires that we know in advance the spectral shift E_0 and the number of Lanczos vectors that cover the entire energy window. This forces us to define the Fermi level by one of the following strategies: (i) to use E_F of the bulk metallic substrate if the atomic model includes a few metal layers, (ii) to use E_F of a known similar system, such as after an intrusion, (iii) to approximate the density of states by a uniform repartition of the on-site energies H_{ii} and establish the link between eigenvalues and their indices, or (iv) to compute

a larger window and allow E_F to be a free parameter when generating the images.[66,67]

C. Tunneling current

Historically, the Tersoff-Hamann (TH) approximation[68] is the first simplified model of a STM. It tells us that the tunneling current $I(\mathbf{r},V)$ is directly related to the local density of states (LDOS) of the isolated sample $\rho_s(E_F^{(s)},\mathbf{r})$ at the Fermi level on the tip apex. This simple interpretation of the STM images is valid in the low-conductance regime when the tip-sample separation is large ($z > 5$ Å) and it assumes that the tip is electronically flat and spherically symmetric. The TH method has successfully explained early experimental results,[69] and it has additionally provided a few insights on the instrument resolution limitations due to the blurring action of the tip. Despite the drastic approximations considered, the TH method is still routinely used in most modern electronic structure methods to generate STM images.[32,34] Once the electronic calculation is completed, the subsequent production of STM images within the TH scheme is very fast, and most of the time, it accurately reveals the most important experimental STM contrasts.

The TH expression can be generalized for tip states $\Psi_t(\mathbf{R})$ with well-defined angular momenta $l > 0$. This would lead to STM images that depend on partial derivative terms $\partial^l\Psi_s/\partial\mathbf{r}^l$,[70] and would represent a first effort to explain the atomic resolution of STM images.[71] However, the modeling of tips with arbitrary geometry requires more detailed numerical simulations. As the Bardeen perturbative formalism[72] depends on a complex coupling between the sample Ψ_s and tip Ψ_t states, this cannot be easily reduced to a TH-like expression when complicated STM tips are considered.

Recently, the perturbative method of Bardeen has regained popularity because of its suitability in describing the STM tunneling regime,[73,74] combined with improvements in accuracy of electronic structures computed by DFT and in efficiency in the calculation of orbital convolutions. Plane separation surfaces as in Fig. 1 usually give satisfying results although the computed wave functions are not sufficiently accurate in the tunneling barrier region far from the sample. To deal with this issue and with highly corrugated samples, Paz *et al.* have used electronic density isosurfaces of the sample as a separation surface[41,75] with only a slight loss in performance.

In the Bardeen[72] (or transfer Hamiltonian) method, the elastic transition probability between *unperturbed* sample states Ψ_s and tip states Ψ_t when a contact is made in the tunneling region is described from first-order time-dependent perturbation theory. This method takes advantage of the peculiar tunneling conditions of the STM and makes the following assumptions:[3,76,77]

(a) chemical and physical interactions between sample and tip do not cause structural deformations to the atomic models;

(b) the barrier has a low conductance ($z > 5$ Å), hence the electrodes are in thermal equilibrium;

(c) inelastic effects and electron-phonon coupling, which generally account for 10% of experimental contrasts, are neglected.

Bardeen found (see also alternate derivations[78,79]) that the tunneling current expression has the form of Fermi's golden rule:[80]

$$I(\mathbf{r},V) = \frac{4\pi e}{\hbar}\int_{-\infty}^{\infty}\rho_s\left(E_F^{(s)}+\epsilon\right)\rho_t\left(E_F^{(t)}-eV+\epsilon\right) \times\left[f_s\left(E_F^{(s)}+\epsilon\right)-f_t\left(E_F^{(t)}-eV+\epsilon\right)\right]|M_{st}(\mathbf{r})|^2 d\epsilon, \tag{12}$$

where ϵ is an integration variable relative to the Fermi levels $E_F^{(s)}$ and $E_F^{(t)}$, and $f_{s,t}(E)$ is the Fermi distribution function. The current density operator is the transfer Hamiltonian that appears in the Bardeen integral:

$$M_{st} = -\frac{\hbar^2}{2m}\int_{\mathcal{S}}(\Psi_s^*\nabla\Psi_t - \Psi_t\nabla\Psi_s^*)d\mathbf{S}. \tag{13}$$

The Bardeen integral (13) is over a separation surface $\mathcal{S}$ that arbitrarily divides the sample and the tip sides.

When the surface density of states arises from the contribution of broadened discrete states Ψ_i as in (3), the tunneling current expression of (12) can be written as

$$I(\mathbf{r},V) = \frac{4\pi e}{\hbar}\sum_{s,t}F_{st}(V)|M_{st}(\mathbf{r})|^2, \tag{14}$$

where $F_{st}(V)$ is the *Fermi factor* between states of energy E_s and E_t at a given V:

$$F_{st}(V) = \int_{-\infty}^{\infty}\rho_s\left(E_F^{(s)}+\epsilon\right)\rho_t\left(E_F^{(t)}-eV+\epsilon\right) \times\left[f_s\left(E_F^{(s)}+\epsilon\right)-f_t\left(E_F^{(t)}-eV+\epsilon\right)\right]d\epsilon. \tag{15}$$

To have a significant contribution to the tunneling current, two states need a strong overlap in real space ($|M_{st}|^2$) and in energy space (F_{st}). The Fermi factor indicates if an elastic transition between two states is possible at a bias V.

Furthermore, spectroscopic computations are straightforward to evaluate in conjunction with the tunneling current:

$$dI/dV(\mathbf{r},V) = \frac{4\pi e}{\hbar}\sum_{s,t}F'_{st}(V)|M_{st}(\mathbf{r})|^2. \tag{16}$$

The STM temperature is usually low enough such as $k_BT \ll \gamma_s+\gamma_t$ and becomes negligible ($T \simeq 0$). Hence, the Fermi factor becomes

$$F_{st}(V) = \int_0^{eV}\rho_s\left(E_F^{(s)}+\epsilon\right)\rho_t\left(E_F^{(t)}-eV+\epsilon\right)d\epsilon. \tag{17}$$

Elastic transitions occur between two broadened states if they are aligned in energy and if they are located in the same energy window [Eqs. (9) and (10)]. Similarly, we can show by applying the Leibniz integration rule to (17) that the bias V influences the tunneling current by changing the energy alignment of pairs of states and by resizing the energy window where $\rho_s\rho_t$ is significant.

The *flat band* limit involves tip states with high broadening ($\gamma_t \gg \gamma_s, \gamma_t \gg eV$) so that $\rho_t(E)$ becomes roughly constant:

$$F_{st}(V) = \rho_t\int_0^{eV}\rho_s\left(E_F^{(s)}+\epsilon\right)d\epsilon \simeq eV\rho_t\rho_s\left(E_F^{(s)}\right), \tag{18}$$

$$F'_{st}(V) = \rho_t\rho_s\left(E_F^{(s)}+eV\right) \simeq e\rho_t\rho_s\left(E_F^{(s)}\right). \tag{19}$$

The right-hand side of Eqs. (18) and (19) is the low bias approximation ($eV \ll \gamma_s$), where the tunneling current depends only on the Fermi level density of states of the sample.

While the Bardeen integral (13) can be computed by expanding the STO basis functions $\psi_{s,t}$ in Gaussian orbitals (STO-nG),[81,82] by expanding the tip molecular orbitals in spherical harmonics $Y_m^l(\hat{\mathbf{R}})$ (with $\mathbf{R} = 0$ on the apex) on the separation surface,[70] or by relating integrals involving $\nabla\psi_i$ to several overlap integrals of higher angular momenta,[83] we will use direct integration on a plane $\mathcal{S}$ in real space. This approach is more efficient for dealing with tips of arbitrary composition.

We choose as the separation surface $\mathcal{S}$ the xy plane in the tunneling region at $Z = (\mu - 1)z$, where $0.2 \leqslant \mu \leqslant 0.8$. By making an explicit translation $\mathbf{r} \equiv (x,y,z)$ of the orbitals Ψ_t during the tip scan, the Bardeen integral becomes a convolution:

$$M_{st}(\mathbf{r}) = -\frac{\hbar^2}{2m}\int_{-y_t}^{y_t}\int_{-x_t}^{x_t}\left[\Psi_s(\mathbf{R}+\mathbf{r})\frac{\partial\Psi_t}{\partial z}(\mathbf{R}) - \Psi_t(\mathbf{R})\frac{\partial\Psi_s}{\partial z}(\mathbf{R}+\mathbf{r})\right], \tag{20}$$

where $\mathbf{R} \equiv (X,Y,Z)$ is the position on the surface $\mathcal{S}$ relative to the apex and where $\Psi_t(\mathbf{R})$ and $\partial\Psi_t/\partial z(\mathbf{R})$ are negligible far from the apex where $|X| > x_t$ or $|Y| > y_t$. By integrating numerically over a uniform grid of resolution $\Delta x = \Delta y$, Eq. (20) becomes a discrete convolution:

$$M_{st}(\mathbf{i}) = -\frac{\hbar^2}{m}\frac{2x_t y_t}{n_X n_Y}\sum_{I,J}\Psi_s[\mathbf{I}+\mathbf{i}]\frac{\partial\Psi_t}{\partial z}[\mathbf{I}] - \Psi_t[\mathbf{I}]\frac{\partial\Psi_s}{\partial z}[\mathbf{I}+\mathbf{i}], \tag{21}$$

where $\mathbf{I} \equiv (I,J,K)$ and $\mathbf{i} \equiv (i,j,k)$ are the grid indices of the tip orbitals Ψ_t and of the scanning zone respectively, and n_X, n_Y, and n_Z are the sizes of the Ψ_t grid along each axis. The Ψ_s and Ψ_t real space grids are obtained from the atomic orbitals ψ_i (4) and from $\partial\psi_i/\partial z$:

$$\frac{\partial\Psi_i}{\partial z} = \sum_{j=1}^{N}\chi_{ij}\frac{\partial\psi_j}{\partial z}, \tag{22}$$

which can be easily derived from (7). Every grid point $\mathbf{R}$ consequently needs $2N$ real space evaluations.

Convolutions like (21) are optimally evaluated in a two-dimensional plane wave basis. By the convolution theorem, we have

$$\mathcal{F}\{M_{st}(\mathbf{i})\} = -\frac{\hbar^2}{m}\frac{2x_t y_t}{n_X n_Y}\left(\mathcal{F}\{\Psi_s[\mathbf{I}]\}\mathcal{F}\left\{\frac{\partial\Psi_t}{\partial z}[\mathbf{I}]\right\} - \mathcal{F}\{\Psi_t[\mathbf{I}]\}\mathcal{F}\left\{\frac{\partial\Psi_s}{\partial z}[\mathbf{I}]\right\}\right), \tag{23}$$

where $\mathcal{F}\{f\}$ is the discrete two-dimensional fast Fourier transform (FFT) of f computed in $O[(n_x+n_X)(n_y+n_Y)\log(n_x+n_X)(n_y+n_Y)]$ order by the FFTW library[84] as compared to $O(n_x n_X n_y n_Y)$ for a direct integration. This (noncircular) fast convolution requires padding the sample grid beyond the primitive scan zone to include the effects of blurring by the finite-size tip. Pixels affected by the periodical extensions of FFTs will simply be discarded. This procedure computes $M_{st}(\mathbf{i})$ for all pixels (x,y) in a single step. Topographic mode consequently requires a predefined grid in z with intervals Δz within which we assume $I(z) \sim \exp(-\alpha z)$. Since the tunneling current is roughly exponential in z, large intervals Δz work well.

The Tersoff-Hamann (TH) approximation[68,85] builds on top of the Bardeen perturbative theory with the additional assumptions of a low temperature ($T \simeq 0$), the *flat band* limit [Eqs. (18) and (19)], and the tip orbitals Ψ_t being roughly spherically symmetric (s type) in the tunneling barrier:

$$\Psi_t(\mathbf{R}) \simeq \frac{1}{kR_0}e^{-k(R-R_0)}, \tag{24}$$

where R_0 is the tip radius and k is the inverse decay length in vacuum. The finite tip size can be shown to filter out the spatial Fourier components b of Ψ_s higher than

$$b \gg \pi\sqrt{\frac{2k}{R_0+Z}}, \tag{25}$$

which gives insight to the STM maximal resolution. The Bardeen integral is then given by (see Ref. 70 for the general case)

$$M_{st}(\mathbf{r}) = A\Psi_s(\mathbf{r}). \tag{26}$$

Inserting (19) and (26) into (16) gives the usual interpretation of STM images:

$$dI/dV(\mathbf{r},V) \propto \rho_s\left(E_F^{(s)}+eV,\mathbf{r}\right) \simeq \rho_s\left(E_F^{(s)},\mathbf{r}\right), \tag{27}$$

$$I\left(\mathbf{r},V\right) \propto \int_0^{eV}\rho_s\left(E_F^{(s)}+\epsilon,\mathbf{r}\right)d\epsilon \simeq V\rho_s\left(E_F^{(s)},\mathbf{r}\right). \tag{28}$$

The differential tunneling conductance is proportional to the Fermi-level local density of states (LDOS) of the sample at the tip apex. In this view, topographic maps $z(I)$ correspond to isosurfaces of $\rho_s(E_F,\mathbf{r})$. This simple result is still widely used today.

D. Image updating

When a small chemical or structural modification of the sample is introduced, most of the data structures of the previous calculation can be efficiently reused to produce an updated image. In this section, we will present the different theoretical considerations we have made to accelerate the generation of an STM image after an intrusion, especially when considering the building of matrices and the matrix diagonalization, and for the evaluation of the tunnel current.

The first step of this strategy is to map the unchanged basis functions to the reference system functions (previous calculation). For being considered identical, two basis functions should have the same parameters such as defined in (8). Assuming that the positions of unchanged atoms stay fixed after the intrusion, we have considered the following cases:

(1) Introducing a vacancy causes the withdrawal of q basis functions centered on this element.

(2) Inserting an interstitial defect or a functional pattern adds p basis functions to the new elements.

(3) Substituting an atom or a group of atoms causes the withdrawal of q and the addition of p basis functions, where

possibly $p = q$ if the elements are in nearby columns of the periodic table.

When constructing the Hamiltonian matrix H (and similarly for S), we can easily obtain an element H_{ij} if ψ_i and ψ_j have antecedents in the reference system. We thus only have to compute p new lines and p new columns in H where ideally $p \ll N$. The first step of matrix formation then goes from $O(N^2)$ complexity to $O(pN)$ which virtually becomes computationally negligible. Furthermore, we note that introducing a vacancy requires no significant computation at this step.

The diagonalization of matrices needs to be performed from scratch with the exception of two cases that apply to large systems. First, when the Fermi level of the reference system has been determined by a direct method, a faster iterative method can be used to diagonalize the matrix after an intrusion. Second, when an eigenvector of the Fermi level of the reference system is used as the initial value of the Lanczos iterations, the algorithm is expected to converge faster. Note that restricting the diagonalization to the perturbed part of the Hamiltonian is not feasible in general for the generalized shift-invert problem with the implicitly restarted Lanczos method. However, this last strategy does not reduce the order of complexity of the method and the diagonalization remains a limiting step.

Finally, the tunneling current (or pixel) must be updated over the entire scanned region since we cannot anticipate the effects of localization or long range interactions on the resulting STM image. This requires the following operations:

(1) Evaluate the basis functions ψ_s (ψ_t, $\partial\psi_s/\partial z$, $\partial\psi_t/\partial z$ for Bardeen) on a grid in real space.

(2) Construct the molecular orbitals Ψ_s (Ψ_t, $\partial\Psi_s/\partial z$, $\partial\Psi_t/\partial z$) with Eqs. (4) and (22).

(3) Compute the convolutions $M_{st}(\mathbf{r})$ (Bardeen only).

(4) Construct the final image plugging $M_{st}(\mathbf{r})$ and $F_{st}(V)$ into Eq. (14).

Operations 2 and 4 depend on the new values of χ_{ij} but are merely linear combinations; they are typically negligible when the number of computed eigenvectors is $n_s \ll 40$. Furthermore, operation 3 is trivial for the Tersoff-Hamann method, and is quite efficient for Bardeen in conjunction with the fast convolution algorithm. The evaluation of $(\partial)\psi_i$ in real space can be substantially alleviated by keeping in memory the grids of the unchanged basis functions of the reference system. This obviously requires that the two scanning grids stay the same during the image updating. Operation 1 drops from $O(N)$ to $O(p)$, and consequently the whole step of computing tunneling current usually becomes negligible.

III. RESULTS AND DISCUSSION

A. Quality of the physical description

This section summarizes the results of our TH and Bardeen calculations on a molecular system made of tetracyanoethylene (TCNE) adsorbed on a Cu(100) surface (see Fig. 2) that we have previously studied.[86] The adsorption of this strong electron acceptor causes a major surface reconstruction and a partial charge transfer that need to be described with our model. We validate our TH and Bardeen results with respect to an experimental STM image, and we make an extensive comparison of the two approaches (TH, Bardeen) to a more rigorous electron scattering technique based on the Landauer-Büttiker formalism previously used for this TCNE/Cu(100) system.

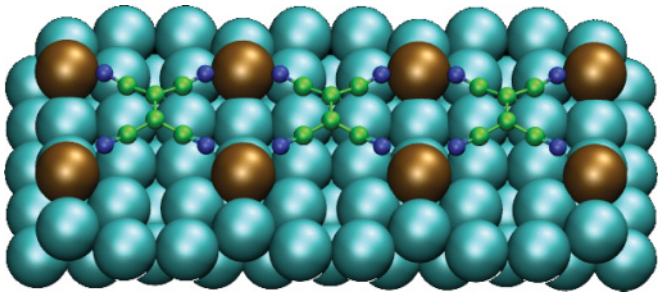

FIG. 2. (Color online) Optimized structural model of a TCNE (C_6N_4) chain on a strongly reshaped Cu(100) surface. This cluster contains three TCNE molecules (green and blue) on two Cu layers (cyan). Highly buckled Cu atoms are outlined (copper). Details on the overlayers structure can be found in Ref. 86.

Figure 3(a) shows the experimental STM image of a TCNE chain obtained with a Pt/Ir tip in topographic mode ($V_0 = 1$ mV, $I_0 = 5$ nA).[87] Characteristic features of the STM contrasts include the main lobe, faint *short legs*, larger *extended legs*, and dark trenches.

Figure 3(b)[86] shows an STM simulation based on a parallel implementation[57] of the Landauer-Büttiker (LB) formalism using the Green's functions technique[55,56] and an extended Hückel Hamiltonian.[60] The atomic model used in this simulation has been obtained from an independent DFT-LDA calculation that reveals a strong reconstruction of the Cu(100) surface following the TCNE adsorption.[86] The tip used in the simulation was made of Pt(111). The presence of the three main characteristic features observed experimentally, in addition to the similarity of the calculated distance based on STM contrasts (7.7 ± 0.2 Å) between extended legs to the experimental value (7.3 ± 0.3 Å), strongly favored a surface reconstruction mechanism rather than a trapping of Cu surface atoms that diffuse near Cu(100) step edges.[86]

Figure 3(c) shows the result of our Bardeen calculation applied on the same reconstructed surface model, with extended Hückel parameters and a Pt(111) tip similar to those in Fig. 3(b). However, the surface model for both sample and tip was limited to two-layer clusters ($\gamma_s = 0.1$ eV, $\gamma_t = 0.5$ eV) as in Fig. 2. Despite the absence of the dark trenches on our simulated image, the Bardeen method successfully accounts for the main lobe, the short legs, and the extended legs, as well as the perpendicular distance between maxima of extended legs (7.3 ± 0.3 Å). This result clearly demonstrates the power of such perturbative approach in qualitatively giving an accurate physical representation of STM contrasts but with many fewer computing resources.

Finally, Fig. 3(d) shows our TH calculation applied to the same structural model. We note the presence of the main lobe and of the short and extended legs. Hence, the calculated local density of states $\rho(E_F^{(s)},\mathbf{r})$ explains correctly the positions of protrusions in the main image. The contrasts above and below the main lobe are however slightly distorted with respect to the experimental image [Fig. 3(a)]. This discrepancy can be

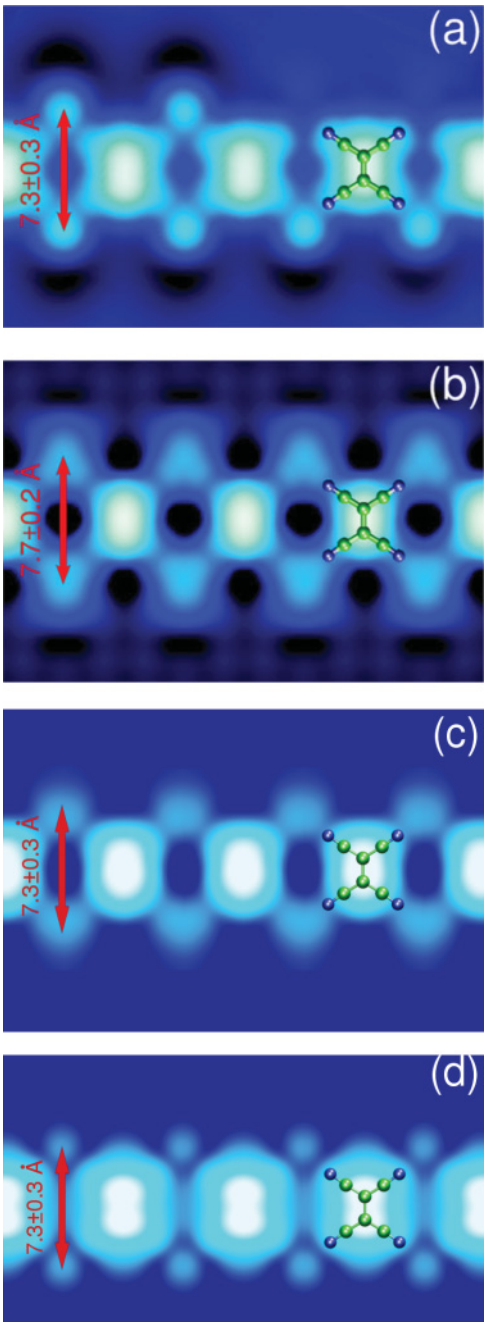

FIG. 3. (Color online) Topographic STM images of a TCNE chain on Cu(100) (a) obtained experimentally with a Pt/Ir tip ($V_0 = 1$ mV, $I_0 = 5$ nA),[87] or calculated with a Pt(111) tip ($V_0 = 1$ mV, $I_0 = 15$ nA) using (b) the LB approach,[86] and the (c) Bardeen and (d) TH methods.

explained by the asymmetry of the d band of the Pt/Ir tip[88] that is neglected in this TH calculation. In fact, if one applies the Bardeen method but explicitly ignores the d band of the tip, we obtain the same result than with the TH method shown in Fig. 3(d).

One significant difference between Bardeen or TH and LB images is the existence of dark areas in the vicinity of the bumped surface Cu atoms. In the case of LB images, previous DFT calculations showed that dark trenches can be associated with a zone of charge density depletion.[86] The absence of these zones in Bardeen and TM images suggests that we may attribute this difference with LB images to our limited atomistic description of the STM tunnel junction used in both TH and Bardeen methods. An alternative mechanism that could contribute to the existence of such dark trenches is related to interference effects between the tip and the substrate.[89,90] Both the Bardeen and TH approaches could, in principle, reproduce interference effects in the tunneling junction if the scatterer is fully enclosed in the substrate or tip regions considered, such as in the present study.[3] Hence, since the effects of interference are taken into account in all of these images (Bardeen, TH, LB), the discrepancy in the description of charge density still constitutes the most reliable explanation for the differences between Bardeen (TH) and LB images.

The main differences between the present Bardeen approach and the LB technique that was used to compute the image in Fig. 3(b) can be summarized by two factors: (i) We use only a partial description of the electronic structure of sample and tip contacts, and (ii) we evaluate the "scattering" of electrons at first order in the tunneling region using Eq. (12).

B. Performance

This section provides additional performance measurements and analysis of our intrusive imaging algorithm. We compare our approach to (1) a parallelized version of the LB[57] method using also tight-binding (TB) Hamiltonians, (2) to the Bardeen method using a special separation surface,[41,75] and (3) to the Bardeen method within a Green's functions framework.[73,74] The performance of our update strategy is compared to complete STM calculations under similar computational conditions.

The creation of the TCNE/Cu(100) image previously shown in Fig. 3(d) requires 9.90 seconds with TH and 16.02 seconds with Bardeen [Fig. 3(c)] theory on one processor, while the LB approach [Fig. 3(b)] has required ~80 hours of total CPU time.[57] Hence, using Bardeen over LB with similar TB Hamiltonians may accelerate the production time for images by about 5 orders of magnitude. Given the very good agreement between the Bardeen method and experimental results, the observed performance is quite interesting.

Table I shows the detailed profiling data of our code according to the main computational steps: (1) matrix formation, (2) diagonalization, and (3) evaluation of the tunneling current. The last column indicates the order of complexity of the operation in $O(\cdot)$ notation. For the Bardeen method, the electronic structure calculations include the tip side which is however negligible compared to the sample side ($N_t = 90 \ll N_s = 1497$).

The diagonalization steps include the initial tridiagonalization in $O(N^3)$ and the bisection eigenvalue search in $O(Nn_s)$, where n_s (n_t) is the number of eigenvalues of the sample (tip) contained in the energy window. As only $n_s = 36$ of the 1497 eigenvalues were computed, the computing time for the bisection operation is virtually eliminated in comparison to the original LAPACK master drivers in $O(N^2)$ (23.30 s) given our index and energy window definition. The complete bisection step usually represents 20% to 90% of the entire diagonalization time.

TABLE I. Performance profiling for the TCNE/Cu(100) calculations (seconds).

	TH	Bardeen	Order
1.a Matrices H,S	0.32	0.33	$O(N^2)$
2.a Tridiagonalization	5.30	5.30	$O(N^3)$
2.b Bisection	0.88	0.88	$O(Nn_s)$
3.a Evaluation of $(\partial)\psi_i$	1.60	4.46	$O(Nn_p)$
3.b Formation of $(\partial)\Psi_i$	1.75	4.07	$O(Nn_sn_p)$
3.c Convolutions $M_{st}(\mathbf{r})$	-	0.77	$O(n_sn_tn_p)$
3.d Image formation	0.05	0.21	$O(n_sn_tn_Vn_p)$
Total	9.90	16.02	

The steps in tunneling current calculation first require the evaluation of the atomic (ψ_i) and molecular (Ψ_i) orbitals, as well as their gradients for the Bardeen method, on a real space grid located on the separation surface containing $n_p \equiv n_x n_y n_z$ pixels. Since n_s generally grows with N when V is fixed, operation 3.a is a limiting step only for small to medium systems ($n_s \ll 40$). The convolution operation specifically applies to the Bardeen method and is never a limiting step. For this system, we have also noted that the FFT convolution algorithm performs better (0.77 s) than a direct numerical integration (26.09 s). Finally, the image formation that combines the Bardeen integrals $M_{st}(\mathbf{r})$ and the Fermi factors $F_{st}(V)$ scales as $O(n_sn_tn_Vn_p)$, where n_V is the number of different applied biases (here $n_V = 1$) and where $n_t = 1$ for TH. As expected, this last operation is not computationally very demanding.

To summarize, using Eq. (3) instead of treating periodic contacts by Green's functions[73,74] allows the following optimizations. The contact resonances in the tunneling barrier $\Psi(E,\mathbf{r})$ are obtained from mixing the surface states $\Psi_i(\mathbf{r})$ close to E in energy. This allows us to evaluate $M_{st}(\mathbf{r})$ only once for each surface states pair. Furthermore, $M_{st}(\mathbf{r})$ does not need to be computed when Ψ_s or Ψ_t are localized far from the tunneling barrier, or when the Fermi factors $F_{st}(V)$ are negligible for all V considered. We choose a separation surface in the xy plane instead of LDOS isosurfaces[41,75] for the following reasons: (i) The convolutions stay practically identical when the separation surface is translated between the sample and the tip at $Z = (\mu - 1)z$ where $0.2 \leqslant \mu \leqslant 0.8$, and (ii) the topographic dependency $I(z)$ is usually well resolved on z grids containing a few (such as two or three) data points.

C. Chemical intrusion

In the present study, we have demonstrated the relevance of the chemical composition on the STM images for the following cases of intrusion: (i) the substitution of an atom or a group, (ii) the withdrawal of an atom or a group, (iii) the functionalization of a site, and (iv) molecular reorganization. Those modifications are generally applicable to both the sample and the tip.[43] As an example, we first considered two chemical intrusions on isolated benzene (C_6H_6), namely the substitution of a C-H group for an N atom to give pyridine (C_5H_5N) and the withdrawal of one and two contiguous H atoms to form phenyl (C_6H_5) or benzyne (C_6H_4). We analyze the gain in performance obtained by our fast image update method.

Figure 4 presents the constant-height STM images of isolated benzene [Fig. 4(a)], pyridine [Fig. 4(b)], phenyl [Figs. 4(c) and 4(e)], and benzyne [Fig. 4(d)] as computed by our intrusive TH implementation. We need to emphasize the fact that a complete STM calculation on the modified system gives the same results (not shown) as when the image is updated following the intrusion approach. For comparison, we also include an STM image of benzene but adsorbed on a Cu(100) surface [Fig. 4(f)] that was obtained with our SPAGS-STM software[57,91] using the LB approach. The differences in contrast between Fig. 4(a) and Fig. 4(f) originate mainly from the interaction of benzene with the underlying copper surface that is absent in Fig. 4(a). The STM images obtained

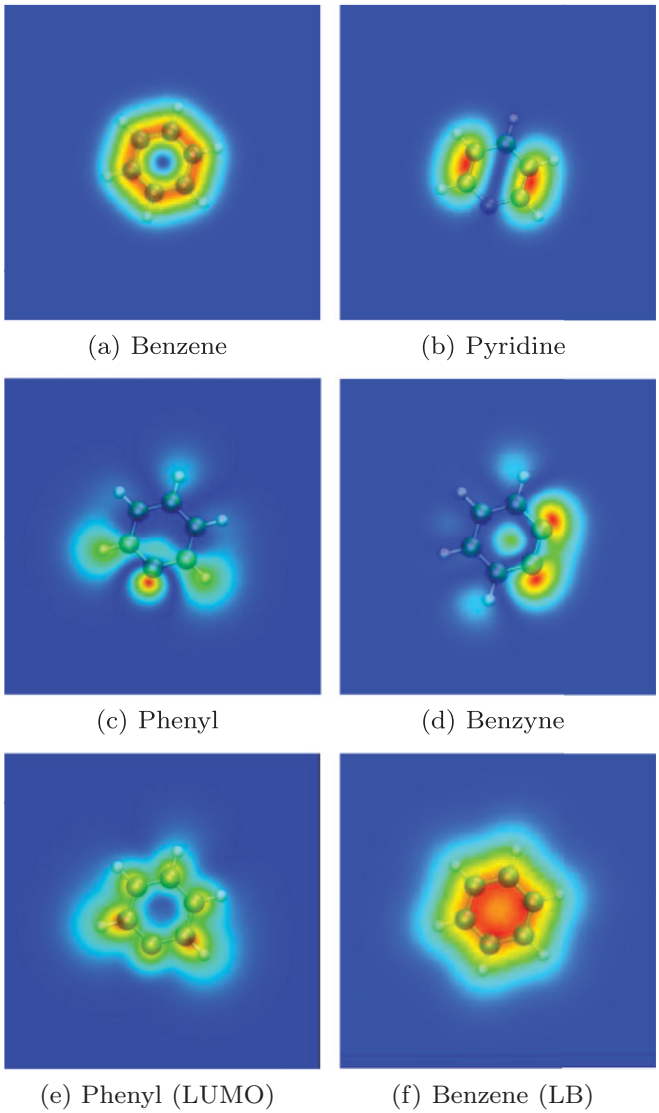

FIG. 4. (Color online) Theoretical constant-height STM images at $V = -0.3$ V of (a) benzene (C_6H_6), (b) pyridine (C_5H_5N), (c) phenyl (C_6H_5), (d) benzyne (C_6H_4), and at $V = +0.3$ V of (e) phenyl computed by our TH implementation on isolated molecules. (f) Image of benzene adsorbed in the "on-top" position on Cu(100) using a Pt(111) tip and the LB approach.[57,91]

within the intrusive framework accurately reproduce the shape of the highest occupied molecular orbitals (HOMO) of the corresponding molecules[92] without performing a complete electronic structure calculation. Our intrusive STM images of the dehydrogenation products of benzene [see Figs. 4(c) and 4(d)] are also consistent with the experimental STM images obtained by Lauhon and Ho[31] for similar systems. A more direct comparison to experimental STM images could tentatively be performed for the case of phenyl [Fig. 4(e) at $V = +0.3$ V] where a similar shape was observed for that species once adsorbed on a Cu(111) surface.[93] Nevertheless, we need to limit our interpretation of chemical intrusion to a qualitative comparison with experimental images for the following reasons. First, we have considered isolated and flat species in our STM calculations while the experimental images of Lauhon and Ho[31] were recorded for adsorbed and tilted species on a Cu(001) surface. More importantly, we have not yet considered molecular relaxation during chemical intrusion, which obviously needs to be taken into account to make any quantitative comparison with experimental results. Although we consider a few samples, they were especially chosen to emphasize the capacity of our intrusive approach to generate STM images of several common species that accurately reproduce the results of a complete STM simulation.

In terms of computing performance, the reference TH calculation on benzene [Fig. 4(a)] has been completed in 60 ms on a single processor. For comparison, the LB calculation on the benzene/Cu(100) system [Fig. 4(f)] requires 1 h of total CPU time. Since the limiting step in the reference calculation is for the evaluation of the basis functions in real space, the updated images having $p = 4$ (0) new basis functions on a total of $N = 29$ (28) for pyridine (benzyne) were generated in less than 10 ms. Such gain of performance is possible on small molecular systems due to the small number of molecular orbitals (here $n_s = 1$) that need to be constructed in operation 3.b (see Table I). For larger systems, a substantially higher gain can be expected since iterative diagonalization techniques such as the Lanczos method can be efficiently used.

D. System size

To illustrate the advantage of the Lanczos method for large systems, we have performed electronic structure calculations and STM simulation on (5,5) carbon nanotubes (CNT) with finite length ranging from 1.23 nm ($N_{\text{atm}} = 100$) to 184.5 nm ($N_{\text{atm}} = 15000$). The STM image of a medium-sized CNT ($N_{\text{atm}} = 500$) computed with the TH approximation is shown in Fig. 5. Identical results are obtained using both diagonalization methods.

Table II shows the percentage of nonzero elements in the S and H matrices, as well as the CPU usage for the direct and the Lanczos diagonalization methods over an energy window of $[E_F, E_F + 0.3\ \text{eV}]$ ($n_s = 7$–1200). In this case, valence electrons of the carbon atom are described by $2s$, $2p$, and $3d$ orbitals for a total of $N = 9N_{\text{atm}}$ basis functions. The missing values in the table correspond to a few test cases where the needs in memory were exceeding the physical limit of the machine. The Fermi level computed by the direct method converges quickly to a single value ($E_F = -11.47$ eV) as the carbon nanotube length increases. This Fermi energy value was used in the Lanczos method for systems with $N_{\text{atm}} > 2500$.

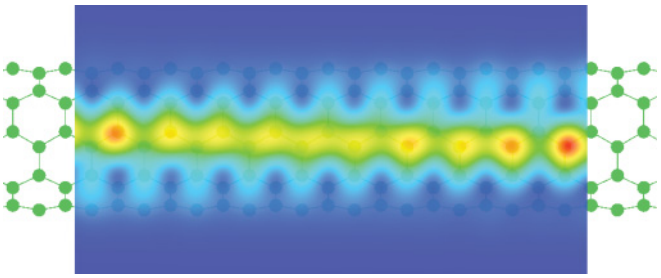

FIG. 5. (Color online) Constant-height STM image ($V = 0.3$ V, $z = 2.8$ Å) of a 500-atom CNT (5,5) computed using the TH approximation.

Assuming a nearest neighbor threshold of $S_{ij} \leqslant 10^{-8}$, the asymptotic percentage of nonzero elements in a CNT (5,5) is $n_{nz} \simeq 126N$. The linear memory usage allows us to deal with systems up to 4 times larger than the dense representation in $n_{nz} = O(N^2)$. The need to track the Lanczos vectors, the nonzero element indices, and the L and U matrices limit the possibility of making further gains. Furthermore, when $N \geqslant 1000$, the iterative method [$O(n_{nz}n_s)$ or $O(N^2)$ for fixed V] is faster than the direct method that becomes limited by the tridiagonalization operation (2.a) in the $O(N^3)$ order. The iterative method may benefit even more from the reduction of the energy window. Such results in performance agree with Li *et al.*[94] on large-scale eigenvalue problems considering that matrix contents can be distributed among the nodes of a parallel machine in order to maximize the system size.[95,96]

IV. CONCLUSIONS

We have developed an interactive scanning tunneling microscopy (STM) simulator that efficiently computes the effects of chemical and structural modifications of adsorbed species on the resulting STM image. First, we have shown that our perturbation theory approach can provide STM images that are qualitatively similar to those of a more rigorous electron scattering technique based on the Landauer-Büttiker formalism. Second, we have demonstrated that the efficiency of Bardeen and Tersoff-Hamann approaches in generating STM images can be substantially improved by introducing the FFT convolution algorithm to evaluate the tunnel current on the surface separation, and the iterative Lanczos method to address

TABLE II. Diagonalization of CNT (5,5) of various sizes.

Size N_{atm}	Nonzeros (%)	Direct Method (s)	Lanczos Method (s)
100	79.30	1.28	1.53
300	36.77	31.02	19.70
500	23.30	128.78	52.31
1500	8.18	3456.80	501.42
2500	4.96	28862.41	1281.03
5000	2.50	–	5682.04
10000	1.25	–	29634.59
15000	0.84	–	–

partial diagonalization of large-scale matrices. Following our general intrusive strategy, we have reduced the computing time to generate an STM image of a modified system by about an order of magnitude with respect to the reference image, while the shape and position of the contrasts of the STM image evaluated in the context of intrusion are virtually identical to an image computed without intrusive features.

ACKNOWLEDGMENTS

This work was supported by the Natural Sciences and Engineering Research Council of Canada (NSERC). Computational resources were provided by the Réseau québécois de calcul de haute performance (RQCHP) and Compute Canada. N.B.-L. is grateful to NSERC for financial support.

*nicolas_boulanger@hotmail.com
†alain.rochefort@polymtl.ca

[1] G. Binnig, H. Rohrer, C. Gerber, and E. Weibel, Phys. Rev. Lett. **49**, 57 (1982).
[2] G. Binnig, H. Rohrer, C. Gerber, and E. Weibel, Appl. Phys. Lett. **40**, 178 (1982).
[3] A. Foster and W. Hofer, *Scanning Probe Microscopy: Atomic Scale Engineering by Forces and Currents* (Springer, 2006).
[4] J. Cerdá, A. Michaelides, M.-L. Bocquet, P. J. Feibelman, T. Mitsui, M. Rose, E. Fomin, and M. Salmeron, Phys. Rev. Lett. **93**, 116101 (2004).
[5] J. Kroger, N. Néel, H. Jensen, R. Berndt, R. Rurali, and N. Lorente, J. Phys. Condens. Matter **18**, 51 (2006).
[6] J. Kröger, H. Jensen, R. Berndt, R. Rurali, and N. Lorente, Chem. Phys. Lett. **438**, 249 (2007).
[7] C. Vericat, G. Andreasen, M. Vela, H. Martin, and R. Salvarezza, J. Chem. Phys. **115**, 6672 (2001).
[8] R. Berndt, R. Gaisch, J. K. Gimzewski, B. Reihl, R. R. Schlittler, W. D. Schneider, and M. Tschudy, Science **262**, 1425 (1993).
[9] R. Berndt, R. Gaisch, W. D. Schneider, J. K. Gimzewski, B. Reihl, R. R. Schlittler, and M. Tschudy, Phys. Rev. Lett. **74**, 102 (1995).
[10] L. Bürgi, O. Jeandupeux, H. Brune, and K. Kern, Phys. Rev. Lett. **82**, 4516 (1999).
[11] V. Madhavan, W. Chen, T. Jamneala, M. Crommie, and N. Wingreen, Science **280**, 567 (1998).
[12] L. Gross, F. Moresco, L. Savio, A. Gourdon, C. Joachim, and K.-H. Rieder, Phys. Rev. Lett. **93**, 056103 (2004).
[13] J. Stroscio and D. Eigler, Science **254**, 1319 (1991).
[14] M. F. Crommie, C. Lutz, and D. Eigler, Science **262**, 218 (1993).
[15] S.-W. Hla, L. Bartels, G. Meyer, and K.-H. Rieder, Phys. Rev. Lett. **85**, 2777 (2000).
[16] P. H. Lippel, R. J. Wilson, M. D. Miller, Ch. Wöll, and S. Chiang, Phys. Rev. Lett. **62**, 171 (1989).
[17] P. Sautet and C. Joachim, Surf. Sci. **271**, 387 (1992).
[18] J. Gimzewski and C. Joachim, Science **283**, 1683 (1999).
[19] W. Ho, Acc. Chem. Res. **31**, 567 (1998).
[20] P. Weiss, Trend Anal. Chem. **13**, 61 (1994).
[21] P. Sautet, Chem. Rev. **97**, 1097 (1997).
[22] G. Briggs and A. Fisher, Surf. Sci. Rep. **33**, 1 (1999).
[23] A. Foster, W. Hofer, and A. Shluger, Curr. Opin. Solid State Mater. **5**, 427 (2001).
[24] N. D. Lang, Phys. Rev. Lett. **56**, 1164 (1986).
[25] I. Tilinin, M. Rose, J. Dunphy, M. Salmeron, and M. Van Hove, Surf. Sci. **418**, 511 (1998).
[26] P. Sautet, Surf. Sci. **374**, 406 (1997).
[27] M. Salmeron, P. Sautet, and J. Dunphy, Surf. Sci. **364**, 335 (1996).
[28] P. Sautet and M.-L. Bocquet, Phys. Rev. B **53**, 4910 (1996).
[29] M. Bocquet and P. Sautet, Surf. Sci. **360**, 128 (1996).
[30] W. Ho, J. Chem. Phys. **117**, 11033 (2002).
[31] L. Lauhon and W. Ho, J. Phys. Chem. A **104**, 2463 (2000).
[32] N. Lorente, M. F. G. Hedouin, R. E. Palmer, and M. Persson, Phys. Rev. B **68**, 155401 (2003).
[33] H. Lesnard, M. Bocquet, and N. Lorente, J. Am. Chem. Soc. **129**, 4298 (2007).
[34] L. Zotti, G. Teobaldi, K. Palotas, W. Ji, H. Gao, and W. Hofer, J. Comput. Chem. **29** (2008).
[35] P. A. Sloan, M. F. G. Hedouin, R. E. Palmer, and M. Persson, Phys. Rev. Lett. **91**, 118301 (2003).
[36] P. Weiss, M. Kamna, T. Graham, and S. Stranicks, Langmuir **14**, 1284 (1998).
[37] V. H. Hallmark, S. Chiang, K.-P. Meinhardt, and K. Hafner, Phys. Rev. Lett. **70**, 3740 (1993).
[38] S. Lemay, J. Janssen, M. van den Hout, M. Mooij, M. Bronikowski, P. Willis, R. Smalley, L. Kouwenhoven, and C. Dekker, Nature (London) **412**, 617 (2001).
[39] D. L. Carroll, P. Redlich, P. M. Ajayan, J. C. Charlier, X. Blase, A. De Vita, and R. Car, Phys. Rev. Lett. **78**, 2811 (1997).
[40] J. C. Dunphy, P. Sautet, D. F. Ogletree, and M. Salmeron, Phys. Rev. B **52**, 11446 (1995).
[41] Ó. Paz, I. Brihuega, J. M. Gómez-Rodriguez, and J. M. Soler, Phys. Rev. Lett. **94**, 056103 (2005).
[42] M. Hove, J. Cerdá, P. Sautet, M. Bocquet, and M. Salmeron, Prog. Surf. Sci. **54**, 315 (1997).
[43] M.-L. Bocquet, J. Cerdá, and P. Sautet, Phys. Rev. B **59**, 15437 (1999).
[44] V. Hallmark and S. Chiang, Surf. Sci. **329**, 255 (1995).
[45] F. Faglioni, C. Claypool, N. Lewis, and W. Goddard III, J. Phys. Chem. B **101**, 5996 (1997).
[46] P. S. Damle, A. W. Ghosh, and S. Datta, Phys. Rev. B **64**, 201403 (2001).
[47] S. N. Yaliraki, M. Kemp, and M. A. Ratner, J. Am. Chem. Soc. **121**, 3428 (1999).
[48] S. Datta, *Quantum Transport: Atom to Transistor* (Cambridge University Press, Cambridge, 2005).
[49] S. Datta, W. Tian, S. Hong, R. Reifenberger, J. I. Henderson, and C. P. Kubiak, Phys. Rev. Lett. **79**, 2530 (1997).
[50] W. Tian, S. Datta, S. Hong, R. Reifenberger, J. Henderson, and C. Kubiak, J. Chem. Phys. **109**, 2874 (1998).
[51] T. Frederiksen, M. Paulsson, M. Brandbyge, and A.-P. Jauho, Phys. Rev. B **75**, 205413 (2007).
[52] A. Korventausta, J. Meyer, and J. Nieminen, Phys. Rev. B **81**, 245426 (2010).
[53] R. Hoffmann, J. Chem. Phys. **39**, 1397 (1963).
[54] D. Kienle, J. Cerdá, and A. Ghosh, J. Appl. Phys. **100**, 043714 (2006).
[55] J. Cerdá, M. A. van Hove, P. Sautet, and M. Salmeron, Phys. Rev. B **56**, 15885 (1997).

[56]J. Cerdá, A. Yoon, M. A. van Hove, P. Sautet, M. Salmeron, and G. A. Somorjai, Phys. Rev. B **56**, 15900 (1997).
[57]B. Janta-Polczynski, J. Cerdá, G. Éthier-Majcher, K. Piyakis, and A. Rochefort, J. Appl. Phys. **104**, 023702 (2008).
[58]I. Guseinov, A. Oezmen, U. Atav, and H. Yueksel, Int. J. Quantum Chem. **67**, 199 (1998).
[59]Z. Romanowski and S. Krukowski, J. Mol. Struct. Theochem **848**, 34 (2008).
[60]J. Cerdá and F. Soria, Phys. Rev. B **61**, 7965 (2000).
[61]G. Golub and C. Van Loan, *Matrix Computations* (Johns Hopkins University Press, Baltimore, 1996).
[62]E. Anderson, Z. Bai, C. Bischof, S. Blackford, J. Demmel, J. Dongarra, J. Du Croz, A. Greenbaum, S. Hammarling, A. McKenney, and D. Sorensen, *LAPACK Users' Guide* (SIAM, Philadelphia, 1999).
[63]C. Lanczos, J. Res. Nat. Bur. Stand. **45**, 255 (1950).
[64]R. Lehoucq, D. Sorensen, and C. Yang, *ARPACK Users' Guide: Solution of Large-Scale Eigenvalue Problems with Implicitly Restarted Arnoldi Methods* (SIAM, Philadelphia, 1998).
[65]J. W. Demmel, S. C. Eisenstat, J. R. Gilbert, X. S. Li, and J. W. H. Liu, SIAM J. Matrix Anal. Appl. **20**, 720 (1999).
[66]W. Tian, S. Datta, S. Hong, R. G. Reifenberger, J. I. Henderson, and C. P. Kubiak, Physica E **1**, 304 (1997).
[67]F. Zahid, M. Paulsson, and S. Datta, in *Advanced Semiconductors and Organic Nano-Techniques* (Elsevier, 2003), pp. 1–41.
[68]J. Tersoff and D. R. Hamann, Phys. Rev. Lett. **50**, 1998 (1983).
[69]G. Binnig, H. Rohrer, C. Gerber, and E. Weibel, Surf. Sci. **131**, L379 (1983).
[70]C. J. Chen, Phys. Rev. B **42**, 8841 (1990).
[71]C. J. Chen, Phys. Rev. Lett. **65**, 448 (1990).
[72]J. Bardeen, Phys. Rev. Lett. **6**, 57 (1960).
[73]W. Hofer and J. Redinger, Surf. Sci. **447**, 51 (2000).
[74]W. Hofer, Prog. Surf. Sci. **71**, 147 (2003).
[75]Ó. Paz and J. Soler, Phys. Status Solidi C **243**, 1080 (2006).
[76]A. D. Gottlieb and L. Wesoloski, Nanotechnology **17**, R57 (2006).
[77]W. Hofer, A. Foster, and A. Shluger, Rev. Mod. Phys. **75**, 1287 (2003).
[78]C. Chen, *Introduction to Scanning Tunneling Microscopy* (Oxford University Press, USA, 1993).
[79]K. Palotas and W. Hofer, J. Phys. Condens. Matter **17**, 2705 (2005).
[80]P. Dirac, Proc. R. Soc. **114**, 243 (1927).
[81]W. Hehre, R. Stewart, and J. Pople, J. Chem. Phys. **51**, 2657 (1969).
[82]R. Stewart, J. Chem. Phys. **50**, 2485 (1969).
[83]C. Roothaan, J. Chem. Phys. **19**, 1445 (1951).
[84]M. Frigo and S. G. Johnson, Proc. IEEE **93**, 216 (2005).
[85]J. Tersoff and D. R. Hamann, Phys. Rev. B **31**, 805 (1985).
[86]S. Bedwani, D. Wegner, M. F. Crommie, and A. Rochefort, Phys. Rev. Lett. **101**, 216105 (2008).
[87]D. Wegner, R. Yamachika, Y. Wang, V. Brar, B. Bartlett, J. Long, and M. Crommie, Nano Lett. **8**, 131 (2008).
[88]D. Papaconstantopoulos, *Handbook of the Band Structure of Elemental Solids* (Plenum Press, New York, 1986).
[89]L. Bartels, G. Meyer, and K.-H. Rieder, Appl. Phys. Lett. **71**, 213 (1997).
[90]J. Nieminen, E. Niemi, and K.-H. Rieder, Surf. Sci. **552**, L47 (2004).
[91]B. Janta-Polczynski, Master's thesis, École Polytechnique de Montréal, 2006.
[92]S. Bachrach, *Computational Organic Chemistry* (John Wiley & Sons Inc., 2007).
[93]S.-W. Hla, L. Bartels, G. Meyer, and K.-H. Rieder, Phys. Rev. Lett. **85**, 2777 (2000).
[94]X. Li, W. Gao, P. Husbands, C. Yang, and E. Ng, J. Phys. Conf. Ser. **16**, 476 (2005).
[95]K. J. Maschhoff and D. C. Sorensen, Lect. Notes Comput. Sc. **1184**, 478 (1996).
[96]X. Li and J. Demmel, ACM T. Math. Software **29**, 110 (2003).